



**Synthesis, Structure and Conduction Mechanism of the
Lithium Superionic Conductor $\text{Li}_{10+\delta}\text{Ge}_{1+\delta}\text{P}_{2-\delta}\text{S}_{12}$**

Journal:	<i>Journal of Materials Chemistry A</i>
Manuscript ID:	TA-ART-10-2014-005231.R1
Article Type:	Paper
Date Submitted by the Author:	31-Oct-2014
Complete List of Authors:	Kwon, Ohmin; Tokyo Institute of Technology, Dept. of Electronic Chemistry Hirayama, Masaaki; Tokyo Institute of Technology, Dept. of Electronic Chemistry Suzuki, Kota; Tokyo Institute of Technology, Kato, Yuki; Toyota Motor Corporation, Battery Research Division Saitoo, Toshiya; Toyota Motor Corporation, Yonemura, Masao; High Energy Accelerator Research Organization, Kamiyama, Takashi ; High Energy Accelerator Research Organization, Kanno, Ryoji; Tokyo Institute of Technology, Dept. of Electronic Chemistry

ARTICLE

Synthesis, Structure, and Conduction Mechanism of the Lithium Superionic Conductor $\text{Li}_{10+\delta}\text{Ge}_{1+\delta}\text{P}_{2-\delta}\text{S}_{12}$

Cite this: DOI: 10.1039/x0xx00000x

Ohmin Kwon,^a Masaaki Hirayama,^a Kota Suzuki,^a Yuki Kato,^b Toshiya Saito,^b Masao Yonemura,^c Takashi Kamiyama,^c Ryoji Kanno*^aReceived 00th January 2012,
Accepted 00th January 2012

DOI: 10.1039/x0xx00000x

www.rsc.org/

A solid solution of the lithium superionic conductor $\text{Li}_{10+\delta}\text{Ge}_{1+\delta}\text{P}_{2-\delta}\text{S}_{12}$ ($0 \leq \delta \leq 0.35$) was synthesized and its structure and ionic conductivity were examined. The highest ionic conductivity value of $1.42 \times 10^{-2} \text{ S cm}^{-1}$ was obtained at 300 K with a sintered pellet of the sample having the highest solid solution lithium content of $\delta = 0.35$. The Arrhenius conductivity curves obtained for this material exhibited a gradual change in slope over the temperature range of 193–373 K and the activation energy for ionic conduction decreased from 26 kJ mol^{-1} below 373 K to 7 kJ mol^{-1} above 573 K, which is typical of highly ionic conducting solids. The crystal structures of the solid solutions were determined using neutron diffraction, and conduction pathways were visualized through analysis applying the maximum entropy method. The lithium distribution was found to disperse significantly throughout a one-dimensional conduction pathway as the temperature was increased from 4.8 K to 750 K. In addition, two-dimensional distribution of lithium along the *ab* plane became apparent at high temperatures, suggesting that the conduction mechanism changes from one-dimensional to three-dimensional with increasing temperature.

1. Introduction

Among the various types of batteries currently under consideration for future applications, the all-solid-state configuration has become a promising candidate for high-energy and high-power-density batteries.^{1–3} The development of materials capable of acting as fast ionic conductors, which can thus be used as solid electrolytes, will play a key role in the realization of these battery systems. The lithium ionic conductor $\text{Li}_{10}\text{GeP}_2\text{S}_{12}$ (LGPS) exhibits extremely high ionic conduction at room temperature, on the order of $10^{-2} \text{ S cm}^{-1}$, a value that is comparable to or much higher than the conductivity values of organic liquid electrolytes such as the ethylene carbonate (EC)/propylene carbonate (PC) system.^{4–6} All solid-state batteries incorporating solid electrolytes show excellent charge-discharge characteristics,⁴ and these power characteristics have been found to be affected by the ionic conductivity of the solid electrolyte, such that higher ionic conductivity leads to significant improvements in the discharge rate of the device.^{2,4}

Although inorganic solid electrolytes offering extremely high lithium ionic conductivities have been developed, further studies clarifying the conduction mechanism and increasing the range of electrolyte materials are still necessary to allow the practical applications of these electrolytes. LGPS is known to have a three-dimensional framework structure composed of one-dimensional chains formed by $\text{Ge}(\text{P})\text{S}_4$ tetrahedra and LiS_6 octahedra with edge sharing along the *c* direction of the tetragonal structure. These one-dimensional chains are connected with each other through PS_4 octahedra by corner sharing. Within this framework structure, lithium occupies the tetrahedral sites along the *c* direction, and the results of neutron diffraction studies have suggested that this contributes to the

ionic conduction process. Theoretical analyses based on first-principles calculations have indicated the presence of a two-dimensional conduction pathway through the lithium in the octahedral coordination environment.^{7,8}

Following the development of this LGPS-type parent structure having extremely high ionic conductivity,^{9–12} it was recognized that similar solid solution systems with different lithium contents might exhibit even higher levels of ionic conduction. In addition, cation and anion substitutions of the LGPS framework structure are also important means of achieving higher ionic conduction values. In the present study, a solid solution with an LGPS-type structure was produced based on a powder synthesis process that offers a practical means of fabricating solid electrolytes. The composition and ionic conductivity of this new solid solution system, $\text{Li}_{10+\delta}\text{Ge}_{1+\delta}\text{P}_{2-\delta}\text{S}_{12}$, were subsequently examined and the conduction mechanism within this material was studied using neutron diffraction analysis.

2. Experimental

The LGPS solid solution was synthesized using a solid-state reaction. In this process, mixtures of P_2S_5 (Aldrich, 99% purity), Li_2S (Nihon Kagaku Kogyo, >99.9% purity), and GeS_2 (Kojundo Chemical Laboratory Co., Ltd., >99.99% purity) were ground in a vibrating mill (CMT, TI-100) for 30 min, pelletized under 220 MPa of pressure, sealed in a silica tube at 30 Pa, and heated at 673 K for 8 h with 2.2 K/min of heating rate and 0.60 K/min of cooling rate. The resulting products were again subjected to grinding and mixing, after which the samples were once more pelletized under 220 MPa, followed by heat treatment at 823 K for 8 h with 3.0 K/min of heating rate and 0.76 K/min of cooling rate. Ionic conductivity values

were measured using samples approximately 10 mm in diameter and 2-3 mm in height which had been pelletized under 165 MPa and sintered at 873 K for 8 h with 3.3 K/min of heating rate and 0.83 K/min of cooling rate. Au powder was coated on the surfaces of samples. The AC impedance values of samples were measured using a frequency response analyzer (National Instrument, nF) by applying 10 mV over the frequency range of 100 Hz to 15 MHz.

X-ray diffraction patterns of the powdered samples were obtained with an X-ray diffractometer (Rigaku, RAD, Ultima or Smart Lab) with CuK α radiation. The diffraction data were collected by applying a 0.02° step width over the 2 θ range from 10° to 80°. Synchrotron X-ray diffraction measurements were performed at the BL02B2 beamline at Spring-8 in Japan, employing a Debye-Scherrer diffraction camera. Specimens were sealed in a quartz capillary (about 0.3 mm diameter) under vacuum. Diffraction data were collected in 0.01° steps over the 2 θ range of 0° to 70.0°. The incident beam wavelength was calibrated using NIST SRM Ceria 640b CeO $_2$ and fixed at 0.59960 Å. Neutron diffraction data were obtained using time-of-flight (TOF) diffractometers: Super HRPD (BL08)¹³ and iMATERIA (BL20)^{13, 14} at the Material and Life science Facility (MLF) of the Japan Proton Accelerator Research Complex (J-PARC). A 6 mm diameter vanadium cell was used and samples were sealed with an indium ring under Ar or He atmospheres. The diffraction data were collected for 12 h at several temperatures; Li $_{10.5}$ Ge $_{1.5}$ P $_{1.5}$ S $_{12}$: 300 K, Li $_{10.35}$ Ge $_{1.35}$ P $_{1.65}$ S $_{12}$: 4.8, 135, and 300 K, Li $_{10.2}$ Ge $_{1.2}$ P $_{1.8}$ S $_{12}$: 300 K and Li $_{10.05}$ Ge $_{1.05}$ P $_{1.95}$ S $_{12}$: 10, 135, 300, 450, and 750 K. Structural parameters were refined using the Rietveld refinement programs Z-Rietveld¹⁵ and RIETAN-FP^{16,17} for neutron and for high-flux synchrotron X-ray diffraction data, respectively. During neutron data analysis, the d region from 1.0 to 3.5 Å was used for the Rietveld analysis. The Z-MEM program was employed during calculations based on the maximum entropy method (MEM).¹⁸ Z-3D¹⁹ was used to

visualize the nuclear density map of the structure. The main text of the article should go here with headings as appropriate.

3. Results and discussion

3.1. Synthesis of the solid solution

The LGPS solid solutions fabricated during this study were based on the Li $_3$ PS $_4$ – Li $_4$ GeS $_4$ pseudo-binary system, and compositions similar to the parent LGPS (Li $_{10}$ GeP $_2$ S $_{12}$) phase were synthesized according to the compositional formula Li $_{10+\delta}$ Ge $_{1+\delta}$ P $_{2-\delta}$ S $_{12}$. Figure 1 (a) shows the X-ray diffraction patterns of the Li $_{10+\delta}$ Ge $_{1+\delta}$ P $_{2-\delta}$ S $_{12}$ compounds synthesized in the present study. The monophasic character of the LGPS phase was observed in those materials in which δ was at or near zero, with a continuous peak shift to lower angles with increasing values of δ , suggesting the formation of a solid solution in the LGPS phase. The lattice parameters were calculated by Rietveld analysis based on the space group $P4_2/nmc$ ⁴ using the synchrotron X-ray diffraction data. Figure 1 (b) shows the lattice parameter changes with the composition of the LGPS phase. The lattice parameters are observed to increase with increasing δ values from zero to 0.50, indicating the formation of a solid solution. A small amount of a Li $_4$ GeS $_4$ impurity phase is observed at $\delta \geq 0.65$ in the Li $_{10+\delta}$ Ge $_{1+\delta}$ P $_{2-\delta}$ S $_{12}$, while a β -Li $_3$ PS $_4$ -type phase (Thio-LISICON phase) is seen in those compositions in which $\delta \leq -0.10$. The compositional range of the solid solution in the Li $_{10+\delta}$ Ge $_{1+\delta}$ P $_{2-\delta}$ S $_{12}$ LGPS phase was determined to span the range $0 \leq \delta \leq 0.50$. The increase in both the lattice parameters and the volume with increasing δ values in Li $_{10+\delta}$ Ge $_{1+\delta}$ P $_{2-\delta}$ S $_{12}$ over the range of $0 \leq \delta \leq 0.50$ is attributed to an increase in the Ge $^{4+}$ (0.390 Å) / P $^{5+}$ (0.17 Å) ratio in the structure.²⁰

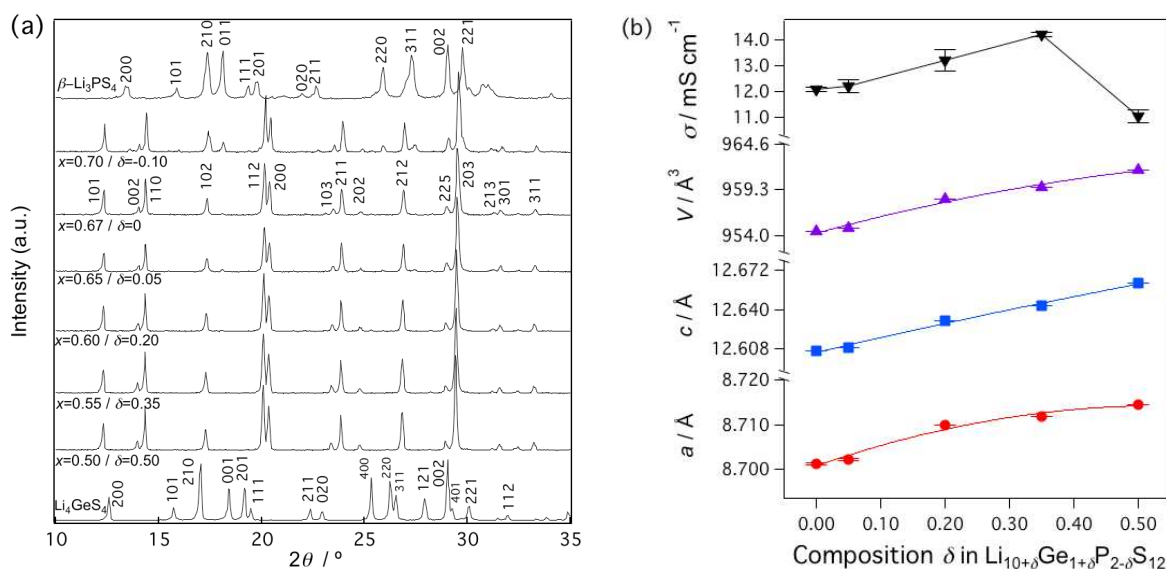


Fig. 1 (a) X-ray diffraction patterns of Li $_{10+\delta}$ Ge $_{1+\delta}$ P $_{2-\delta}$ S $_{12}$ ($-0.10 \leq \delta \leq 0.50$) ($0.50 \leq x \leq 0.70$ in Li $_{4-x}$ Ge $_{1-x}$ P $_x$ S $_4$). A single LGPS phase was obtained for the compositions in which $0 \leq \delta \leq 0.35$ ($0.55 \leq x \leq 0.67$ in Li $_{4-x}$ Ge $_{1-x}$ P $_x$ S $_4$), while β -Li $_3$ PS $_4$ -type and Li $_4$ GeS $_4$ -type phases were observed in materials in which $\delta < 0$ and $\delta > 0.35$ ($x > 0.67$ and $x < 0.55$), respectively. **(b)** Lattice parameters of Li $_{10+\delta}$ Ge $_{1+\delta}$ P $_{2-\delta}$ S $_{12}$ ($0 \leq \delta \leq 0.50$) ($0.50 \leq x \leq 0.67$ in Li $_{4-x}$ Ge $_{1-x}$ P $_x$ S $_4$) as calculated from synchrotron X-ray diffraction measurements at 300 K.

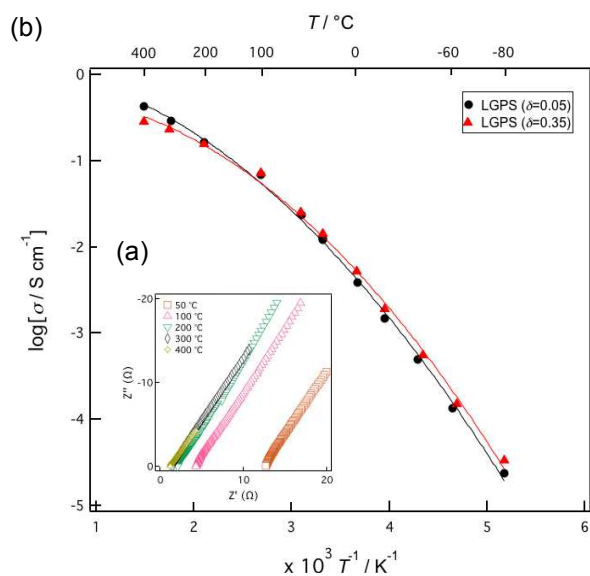


Fig. 2 (a) Impedance plots obtained for $\text{Li}_{10+\delta}\text{Ge}_{1+\delta}\text{P}_{2-\delta}\text{S}_{12}$ ($\delta = 0.35$) over a range of temperatures. (b) Arrhenius plots of the ionic conductivity values of $\text{Li}_{10+\delta}\text{Ge}_{1+\delta}\text{P}_{2-\delta}\text{S}_{12}$ ($\delta = 0.05$ and 0.35).

3.2. Ionic conductivity

Figure 2 (a) presents typical impedance plots obtained from the solid solutions in the form of sintered pellets at various temperatures. These plots only exhibit a spike in the low frequency region, corresponding to the contributions of the electrode components.²¹ As the contributions from the bulk and grain boundary components could not be separated in the temperature range measured during the present study, the reported conductivity values represent the sum total of the grain and bulk contributions. Figure 2 (b) shows Arrhenius plots of the conductivity values measured for two solid solutions. No differences in conductivity were observed during the heating and cooling of both samples, demonstrating that these compositions are stable over the temperature range measured in the present study. The highest ionic conductivity value of $1.42 \times 10^{-2} \text{ S cm}^{-1}$ at 300 K was obtained for the composition in which δ was 0.35, and this conductivity exceeds the value of $1.20 \times 10^{-2} \text{ S cm}^{-1}$ reported previously for such materials.⁴ The activation energies calculated over the temperature range of 193–373 K for the compositions with δ values of 0.05 and 0.35 were 27 and 26 kJ mol^{-1} , respectively. At temperatures above 373 K, the Arrhenius plots exhibit a change in slope and the

activation energy values calculated between 573 and 673 K decrease to 12 and 7 kJ mol^{-1} for these same compositions. The decrease in the activation energy at higher temperatures is a well-known phenomenon associated with highly ionic conducting solids and is sometimes referred to as a diffuse phase transition,²² although it is not yet clearly understood. The LGPS solid solutions show an extremely high ionic conduction state above 373 K.

When assessing the practical applicability of highly ionic conducting materials as solid electrolytes in all solid-state batteries, the conductivity of pressed pellets of the powdered samples is one of the most important parameters in terms of estimating the resistivity of composite electrodes and electrolytes. The ionic conductivity values of pressed powder samples were therefore measured at room temperature. The samples were each pressed under a pressure of 165 MPa and their conductivity values were determined using the AC impedance method. The impedance plots were each composed of a semi-circular region and a spike, corresponding respectively to the bulk/grain boundary and electrode contributions. In this respect, the plots were similar to those produced by sintered pellets and the conductivity values of the bulk/grain boundary are plotted as a function of the composition in Figure 3. The conductivity values are seen to change with variations in the composition, and the highest ionic conductivity of $6.09 \times 10^{-3} \text{ S cm}^{-1}$ was obtained at a δ value of 0.35, corresponding to the sintered pellet composition that exhibited the highest conductivity. On the other hand, ionic conductivity of $\delta = 0.50$, which is expected to be highest value, showed a lower value than that expected in the solid solution. This might originate from a small amount of impurities such as $\beta\text{-Li}_3\text{PS}_4$ although it is hardly detected by XRD.

3.3 Structural analysis using neutron diffraction data

Structural analysis was carried out based on a previously reported model incorporating three lithium sites (Li1 at 16h: x, y, z ; Li2 at 4d: $1, 1/2, z$; Li3 at 8f: $x, x, 0$), together with an Li4 site (Li4 at 4c: $0, 0, z$) proposed as the result of molecular dynamics simulations.²³ The existence of the Li4 site was assessed using the neutron diffraction data acquired at 4.8 K for $\text{Li}_{10.35}\text{Ge}_{1.35}\text{P}_{1.65}\text{S}_{12}$, and the difference in the Fourier map confirmed the presence of lithium at this site. The structural models incorporating the Li4 site in $\text{Li}_{10.35}\text{Ge}_{1.35}\text{P}_{1.65}\text{S}_{12}$ ($\delta = 0.35$) and $\text{Li}_{10.05}\text{Ge}_{1.05}\text{P}_{1.95}\text{S}_{12}$ ($\delta = 0.05$) also provided lower structural reliability (R) factors than those without the Li4 site; for example, S^2 and R_{wp} values were improved from 2.03 and 3.43% to 1.75 and 3.06%, respectively. Table 1 summarizes the R factors and the refined parameters for $\text{Li}_{10.35}\text{Ge}_{1.35}\text{P}_{1.65}\text{S}_{12}$ at room temperature, while Figure 4 provides the Rietveld refinement pattern obtained for $\text{Li}_{10.35}\text{Ge}_{1.35}\text{P}_{1.65}\text{S}_{12}$ at 300 K as an example.

Table 1. Comparison of reliability factors for $\text{Li}_{10.35}\text{Ge}_{1.35}\text{P}_{1.65}\text{S}_{12}$ ($\delta = 0.35$) at 300 K.

	Model with a Li4 site	Model without a Li4 site
R_{wp}	3.06%	3.43%
R_{p}	2.52%	2.77%
R_{e}	2.32%	2.41%
R_{b}	8.58%	11.0%
R_{f}	5.83%	8.25%
S^2	1.75	2.03

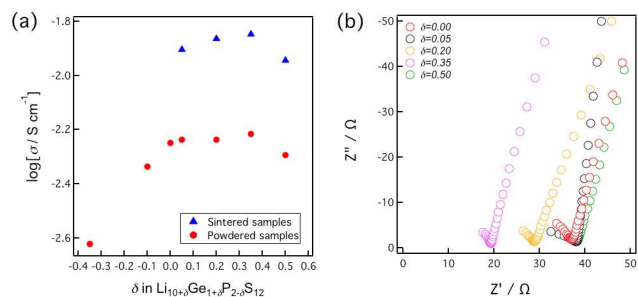


Fig. 3 (a) Dependence of room temperature ionic conductivities of pressed powder samples on composition. (b) Room temperature impedance plots obtained for powder samples.

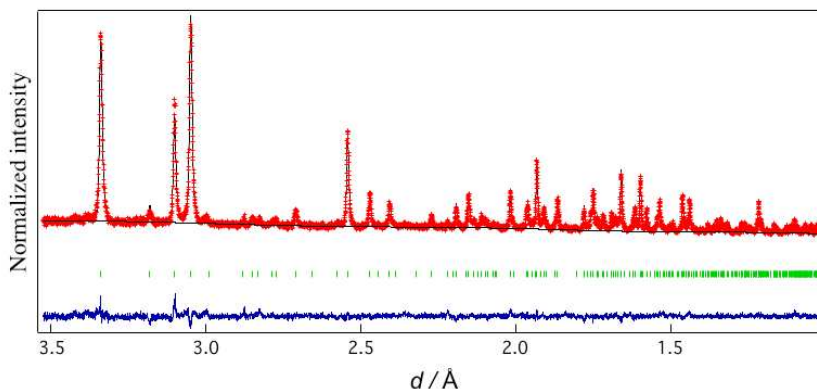


Fig. 4 Neutron Rietveld refinement pattern for $\text{Li}_{10.35}\text{Ge}_{1.35}\text{P}_{1.65}\text{S}_{12}$ at 300 K. Red: observed intensities; black: calculated intensities; blue: difference plot. The green markers indicate the positions of the diffraction lines.

Table 2. Rietveld refinement results for $\text{Li}_{10.35}\text{Ge}_{1.35}\text{P}_{1.65}\text{S}_{12}$ ($\delta = 0.35$) at 300 K.

Atom	Site	g	x	y	z	$U / \text{\AA}^2$
Ge(1)	4d	0.675 (12)	0	1/2	0.6885 (10)	0.046
P(1)	4d	0.325 (12)	= $x(\text{Ge}1)$	= $y(\text{Ge}1)$	= $z(\text{Ge}1)$	= $B(\text{Ge}1)$
Ge(2)	2b	0.00 (2)	0	0	1/2	0.046
P(2)	2b	1.00 (2)	= $x(\text{Ge}2)$	= $y(\text{Ge}2)$	= $z(\text{Ge}2)$	= $B(\text{Ge}2)$
S(1)	8g	1	0	0.1920 (2)	0.4090 (2)	0.046
S(2)	8g	1	0	0.2958 (2)	0.0989 (2)	0.048
S(3)	8g	1	0	0.7005 (3)	0.7885 (2)	0.035
Li(1)	16h	0.473 (11)	0.2477 (9)	0.2616 (13)	0.2018 (11)	0.108
Li(2)	4d	1	0	1/2	0.9524 (4)	0.060
Li(3)	8f	0.75 (2)	= $y(\text{Li}3)$	0.2463 (4)	0	0.118
Li(4)	4c	0.77 (2)	0	0	0.2585 (7)	0.077

Atom	$U_{11} / \text{\AA}^2$	$U_{22} / \text{\AA}^2$	$U_{33} / \text{\AA}^2$	$U_{12} / \text{\AA}^2$	$U_{13} / \text{\AA}^2$	$U_{23} / \text{\AA}^2$
Ge(1)	0.052 (10)	0.044 (14)	0.043 (13)	0	0	0
P(1)	= $U_{11}(\text{Ge}1)$	= $U_{22}(\text{Ge}1)$	= $U_{33}(\text{Ge}1)$	= $U_{12}(\text{Ge}1)$	= $U_{13}(\text{Ge}1)$	= $U_{23}(\text{Ge}1)$
Ge(2)	= $U_{22}(\text{Ge}2)$	0.038 (11)	0.062 (3)	0	0	0
P(2)	= $U_{11}(\text{Ge}2)$	= $U_{22}(\text{Ge}2)$	= $U_{33}(\text{Ge}2)$	= $U_{12}(\text{Ge}2)$	= $U_{13}(\text{Ge}2)$	= $U_{23}(\text{Ge}2)$
S(1)	0.078 (2)	0.023 (2)	0.038 (3)	0	0	0.014 (10)
S(2)	0.055 (2)	0.036 (2)	0.052 (3)	0	0	-0.010 (10)
S(3)	0.044 (2)	0.009 (2)	0.052 (2)	0	0	0.002 (2)
Li(1)	0.074 (8)	0.050 (8)	0.20 (2)	0.019	-0.097 (11)	-0.059 (11)
Li(2)	0.104 (4)	0.051(6)	0.024 (5)	0	0	0
Li(3)	= $U_{22}(\text{Li}3)$	0.048 (5)	0.259 (11)	-0.0335 (3)	= $U_{23}(\text{Li}3)$	-0.0929 (4)
Li(4)	0.026 (9)	0.096 (11)	0.108 (10)	0	0	0

Space group $P4_2/nmc$, $a = 8.713023$ (5) \AA , $c = 12.639695$ (11) \AA , $R_{\text{wp}} = 3.06$ %, $R_p = 2.52$ %.

Note: The form of the anisotropic temperature factor is $\exp[-2p^2(h^2a^*U_{11} + k^2b^*U_{22} + l^2c^*U_{33} + 2hka^*b^*U_{11} + 2hla^*c^*U_{13} + 2klb^*c^*U_{23})]$

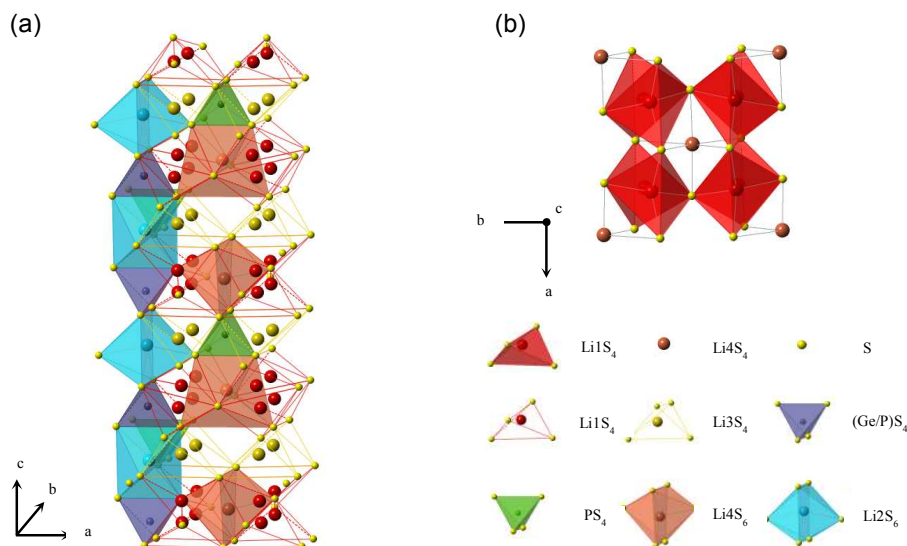


Fig. 5 (a) Structure of $\text{Li}_{10+\delta}\text{Ge}_{1+\delta}\text{P}_{2-\delta}\text{S}_{12}$. $\text{Li}_2(4d)\text{S}_6$ octahedra and $(\text{Ge}/\text{P})(4d)\text{S}_4$ tetrahedra form a one-dimensional framework with $\text{P}(2b)\text{S}_4$ tetrahedra situated between the Li_2S_6 octahedra by corner sharing to connect the one-dimensional chains, thus forming a three-dimensional framework structure. (b) Coordination of $\text{Li}_4(4c)\text{S}_6$ octahedra within the structure. Each $\text{Li}_4(4c)\text{S}_6$ octahedron shares its four edges with $\text{Li}_1(16h)\text{S}_4$ tetrahedra sites.

Figure 5 provides the structure of $\text{Li}_{10.35}\text{Ge}_{1.35}\text{P}_{1.65}\text{S}_{12}$ ($\delta = 0.35$) as determined in the present study. At $\delta = 0.35$, the $4d$ site is occupied by Ge and P with a Ge/P ratio of 0.675/0.325. The framework of $\text{Li}_{10}\text{GeP}_2\text{S}_{12}$ is composed of $(\text{Ge}/\text{P})\text{S}_4$ tetrahedra and Li_2S_6 octahedra in $4d$ sites, connected to one another by edge sharing. The one-dimensional connections between the Li_1S_4 and Li_3S_4 tetrahedra are located at the $16h$ and $8f$ sites, forming a one-dimensional tunnel along the c -axis. The Li4 site introduced in this study is located at the $4c$ site with a fractional coordinate ($z \sim 0.2585$) and the Li4 is connected to six sulfide ions with distances of 2.5(Li4-S1), 2.7(Li4-S2), and 3.3 (Li4-

S3) Å and is situated near the center of eight Li1 sites (see Figure 5) with distances between the Li1 and Li4 sites of $3.2(\times 4)$ and $3.1(\times 4)$ Å. The Li_4S_6 octahedra are also connected to PS_4 tetrahedra by edge sharing along the c direction and to four Li_2S_6 octahedra and two Ge_1S_4 tetrahedra by corner sharing.

3.4. Ionic conduction mechanism

The lithium conduction mechanism was investigated based on neutron diffraction analysis. After a one-dimensional conduction pathway was proposed along the c -axis,⁴ three-dimensional conduction together with the one-dimensional pathway was indicated^{8, 23} based on the results of molecular dynamics (MD) simulations. Furthermore, recent single-crystal

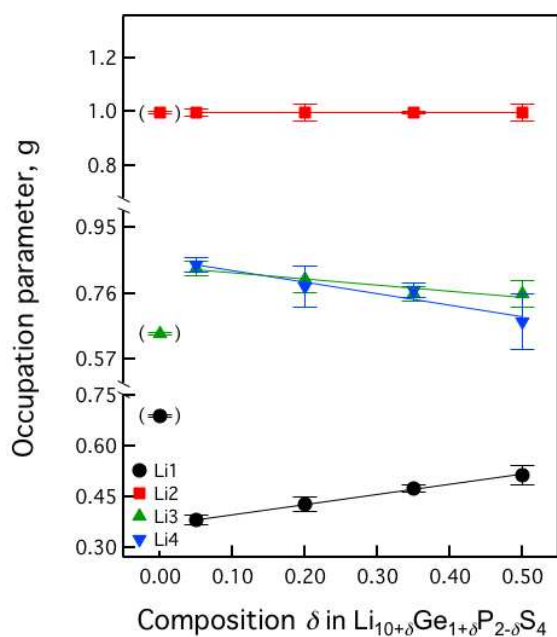


Fig. 6 The occupation parameter, g , at each Li site in $\text{Li}_{10+\delta}\text{Ge}_{1+\delta}\text{P}_{2-\delta}\text{S}_{12}$ as a function of δ . The values at $\delta = 0.0$ are taken from ref 4.

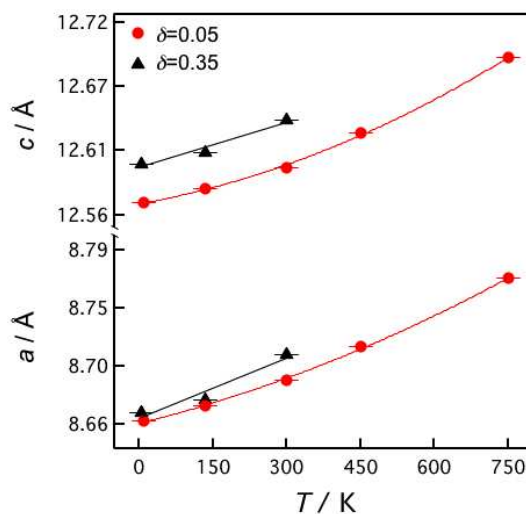


Fig. 7 Temperature dependencies of $\text{Li}_{10+\delta}\text{Ge}_{1+\delta}\text{P}_{2-\delta}\text{S}_{12}$ ($\delta = 0.05$ and 0.35) ($x = 0.55$ and 0.65 in $\text{Li}_{4-x}\text{Ge}_{1-x}\text{P}_x\text{S}_4$) lattice parameters, as calculated from neutron diffraction measurements. The temperature ranges for the $\delta = 0.05$ and 0.35 materials were $4.8 \text{ K} \leq T \leq 300 \text{ K}$ and $10 \text{ K} \leq T \leq 750 \text{ K}$, respectively.

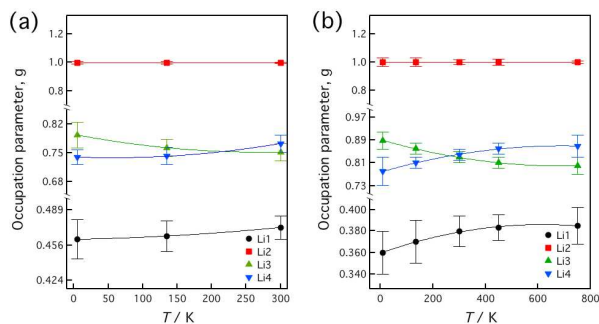


Fig. 8 The occupation parameter, g , at each Li site in (a) $\text{Li}_{10.35}\text{Ge}_{1.35}\text{P}_{1.65}\text{S}_{12}$ ($\delta = 0.35$ in $\text{Li}_{10+\delta}\text{Ge}_{1+\delta}\text{P}_{2-\delta}\text{S}_{12}$) and (b) $\text{Li}_{10.05}\text{Ge}_{1.05}\text{P}_{1.95}\text{S}_{12}$ ($\delta = 0.05$ in $\text{Li}_{10+\delta}\text{Ge}_{1+\delta}\text{P}_{2-\delta}\text{S}_{12}$) as a function of temperature over the ranges of 4.8–300 K and 10–750 K, respectively.

analysis using X-ray diffraction has indicated that three-dimensional motion of lithium ions contributes to the ionic conduction.²⁴ Figure 6 shows the effects of variation in composition on the occupation parameter, g , at each Li site in $\text{Li}_{10+\delta}\text{Ge}_{1+\delta}\text{P}_{2-\delta}\text{S}_{12}$. The g value of the Li1 site increased while those of the Li3 and Li4 sites decreased with increasing values of δ . These behaviors indicate that the lithium ion distribution at these sites changes with the lithium ion distributions are associated with higher lithium composition and that more highly disordered (or uniform) contents. This may correspond to slightly higher lithium ionic conduction for the composition in which $\delta = 0.35$. The total amount of lithium distributed along the Li1 and Li3 conduction pathways increased from 12.7 to 13.5 with increasing values of δ from zero to 0.35. Slightly higher ionic conductivity was observed for the composition in which $\delta = 0.35$, and this might be the result of a higher amount of lithium in the one-dimensional conduction pathway in the structure.

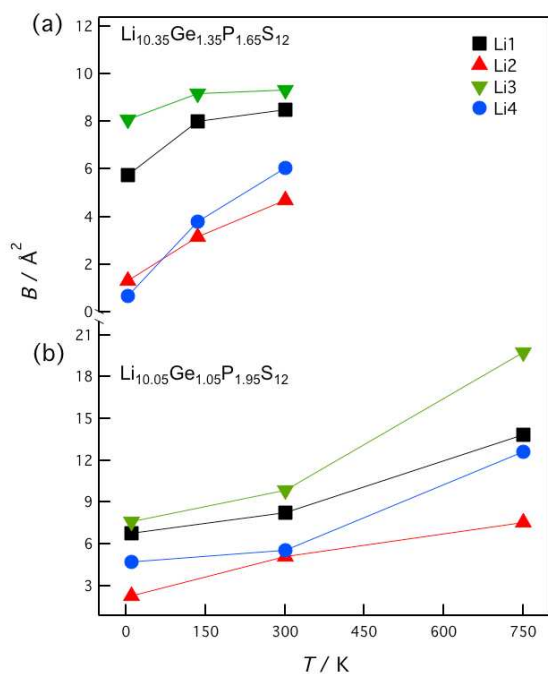


Fig. 9 Temperature dependencies of the isotropic displacement parameters of each Li site in (a) $\text{Li}_{10.35}\text{Ge}_{1.35}\text{P}_{1.65}\text{S}_{12}$ ($\delta = 0.35$) and (b) $\text{Li}_{10.05}\text{Ge}_{1.05}\text{P}_{1.95}\text{S}_{12}$ ($\delta = 0.05$), as measured over the temperature ranges of 4.8–300 K and 10–750 K, respectively.

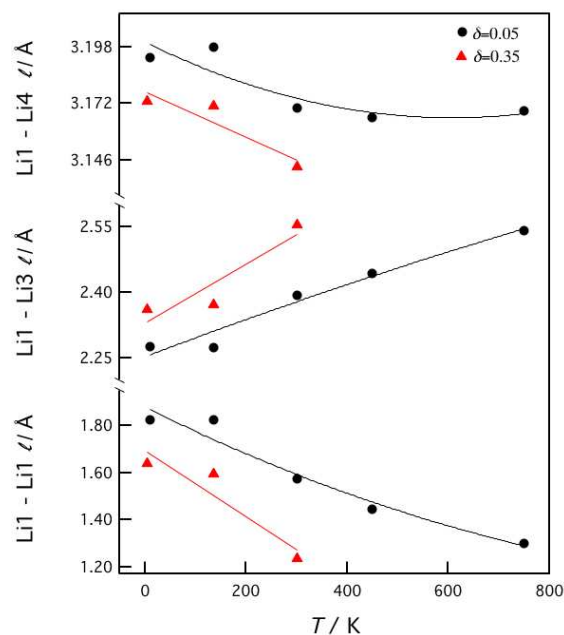


Fig. 10 Temperature dependencies of the atomic distances between Li1 and Li1, and Li1 and Li3 for the compositions $\text{Li}_{10.35}\text{Ge}_{1.35}\text{P}_{1.65}\text{S}_{12}$ ($\delta = 0.35$) and $\text{Li}_{10.05}\text{Ge}_{1.05}\text{P}_{1.95}\text{S}_{12}$ ($\delta = 0.05$).

The temperature dependencies of the lattice parameters were assessed for the compositions in which $\delta = 0.05$ and 0.35, based on synchrotron X-ray diffraction and neutron diffraction analyses. Figure 7 shows the lattice parameter changes with temperature for both samples. The lattice parameters and the volume are seen to have increased with increasing temperature up to 750 K, although no significant phase changes were observed. Figure 8 shows the temperature dependence of the occupation parameter, g , at each Li site in $\text{Li}_{10.35}\text{Ge}_{1.35}\text{P}_{1.65}\text{S}_{12}$ and $\text{Li}_{10.05}\text{Ge}_{1.05}\text{P}_{1.95}\text{S}_{12}$, as measured over the temperature ranges of 4.8–300 K and 10–750 K, respectively. For both compositions, the g value for the Li2 site was constant at 1.0 throughout the entire temperature range, indicating that the Li2 sites form a framework structure with the GeS_4 and PS_4 tetrahedra. In contrast, the g values of the Li1 and Li4 sites increased while that of the Li3 site decreased with increasing temperature. These slight changes in the occupation parameters with temperature may suggest that these sites contribute to the lithium ionic conduction. The g value of the Li3 site decreased and that of Li1 site increased with increasing temperature, which corresponds to more highly disordered lithium distributions at higher temperatures. The temperature dependence of the total quantity of lithium ions in the unit cell was calculated by the MD simulation method²³ and the occupation parameters and thermal evolution of these parameters were found to be quite consistent with those determined for the composition $\text{Li}_{10.35}\text{Ge}_{1.35}\text{P}_{1.65}\text{S}_{12}$ based on neutron diffraction data.

Figure 9 shows the temperature dependence of the isotropic displacement parameter of each Li site in $\text{Li}_{10.35}\text{Ge}_{1.35}\text{P}_{1.65}\text{S}_{12}$ ($\delta = 0.35$) and $\text{Li}_{10.05}\text{Ge}_{1.05}\text{P}_{1.95}\text{S}_{12}$ ($\delta = 0.05$), as assessed over the temperature ranges of 4.8–300 K and 10–750 K, respectively. These isotropic displacement parameters were calculated from the final anisotropic displacement parameters. For both compositions, the B values for the Li2 site were lower than those of the other Li sites, indicating that the Li2 sites form the framework structure along with the GeS_4 and PS_4 tetrahedra.

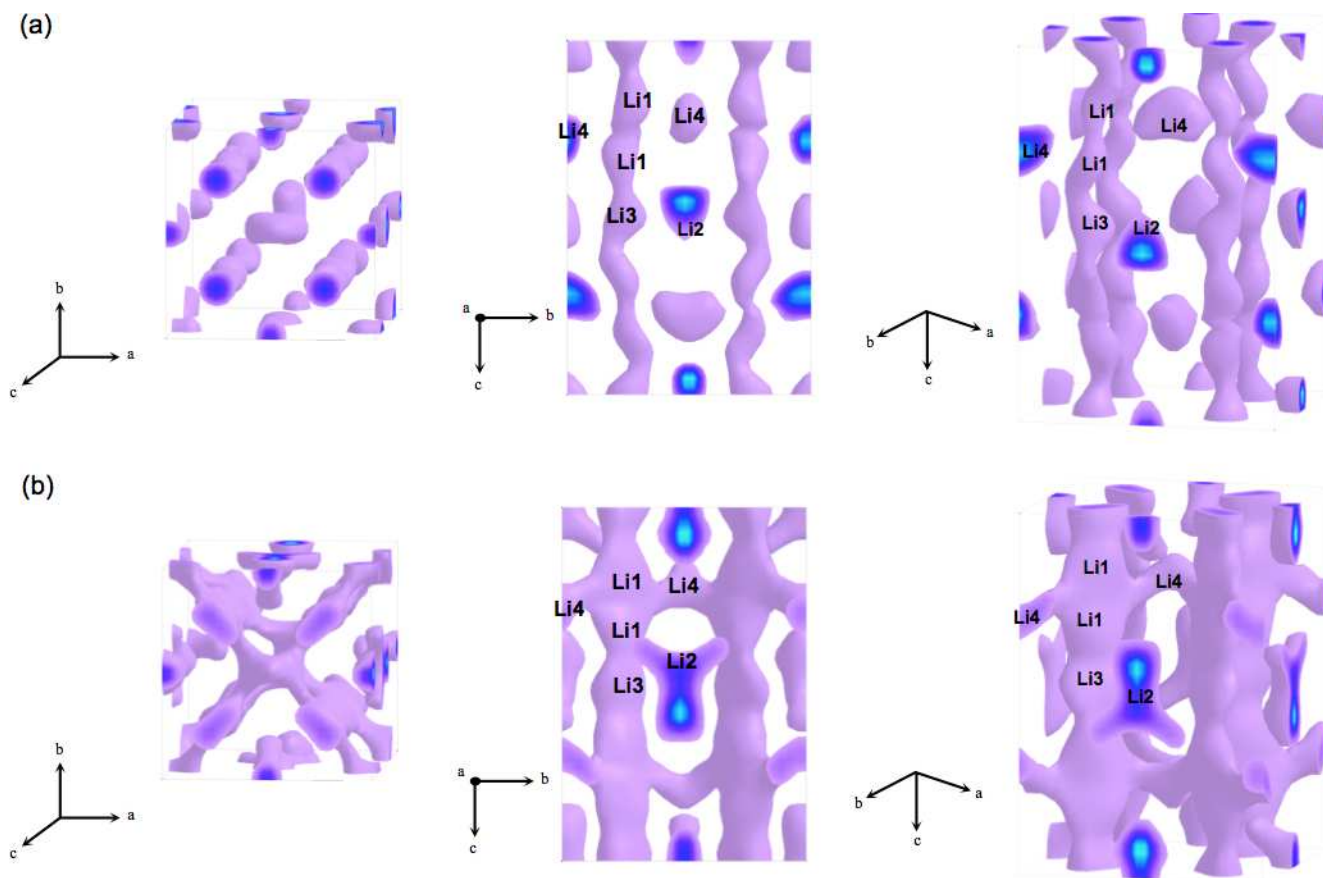


Fig. 11 Atomic distributions in the $\text{Li}_{10.05}\text{Ge}_{1.05}\text{P}_{1.95}\text{S}_{12}$ ($\delta = 0.05$) unit cell at 100 K (a) and 750 K (b). The probability of an atom being present is indicated only for the negative scattering powers, which corresponds to the lithium ion distribution in the unit cell.

The B values of the Li1 and Li3 sites increase with temperature from 4.8–10 K to 300 K and become almost constant above 300 K. These behaviors are consistent with the previous indications that these two sites participate in lithium ionic conduction within the structure. Higher B values at these Li1 and Li3 sites also suggest that these sites make a contribution to Li ion conduction. In contrast, the B value of the Li4 site increases from 10 to 300 K and becomes quite large value at 750 K, and so the Li4 site is expected to play a significant role in ionic conduction at high temperatures.

Figure 10 presents the temperature dependencies of the atomic distances between Li1 and Li1, and Li1 and Li3 for the compositions of $\text{Li}_{10.35}\text{Ge}_{1.35}\text{P}_{1.65}\text{S}_{12}$ ($\delta = 0.35$) and $\text{Li}_{10.05}\text{Ge}_{1.05}\text{P}_{1.95}\text{S}_{12}$ ($\delta = 0.05$). In the case of both compositions, the Li1-Li1 distances decrease and the Li1-Li3 distances increase with increasing temperature. The Li1-Li1 distance approaches 0.13 nm at 300 and 750 K for the $\delta = 0.05$ and 0.35 materials, a value that is close to twice the Li^+ ionic radius in tetrahedral coordination (0.59 Å),²⁰ suggesting that these two Li sites are situated close to one another. The increase in the occupation parameter at the Li1 site and the decrease in the Li1-Li1 distance with increasing temperature point to an elevated extent of lithium disordering along these Li1 sites. The decrease in the g parameters at the Li3 sites and the increase in the Li4 and Li1 sites with an expansion of the Li1-Li3 distance might correspond to a lithium site change from the Li3 to the Li1 and Li4 sites. This result indicates that the conduction mechanism changes from a one-dimensional -

Li1-Li3-Li1-Li1- pathway to a two-dimensional -Li1-Li4-Li1-Li1- pathway. However, the thermal parameters associated with the Li1 and Li3 sites are larger than those of the Li4 sites below 300 K, which may indicate that the one-dimensional conduction pathway is still dominant below room temperature.

Lithium ion distribution was visualized using the MEM analysis in conjunction with the neutron diffraction data obtained for $\text{Li}_{10.05}\text{Ge}_{1.05}\text{P}_{1.95}\text{S}_{12}$ ($\delta = 0.05$) ($x = 0.65$ in $\text{Li}_{4-x}\text{Ge}_{1-x}\text{P}_x\text{S}_4$) at 100 and 750 K. Figure 11 shows the atomic distribution in the unit cell, in which the probability of an atom being present is represented only for the negative scattering powers, which corresponds to the lithium ion distribution in the unit cell. These probabilities were calculated using an isosurface level of 0.08 for the structure at both temperatures. At 100 K, the Li1, Li1, and Li3 sites are connected along the c-axis, while the other lithium sites (the Li2 and Li4 sites) are isolated from each other. This indicates that the one-dimensional conduction pathway represents the primary means of lithium ion conduction at 100 K. The one-dimensional conduction pathway along the c-axis becomes more evident at 750 K. In addition to the one-dimensional connection between the Li1, Li1, and Li3 sites, continuous lithium distribution between the Li1 and Li4 sites is also now observed. These results demonstrate that the lithium ion conduction takes on a three-dimensional character, as opposed to one-dimensional, at higher temperatures. The existence of three-dimensional ionic conduction at high temperatures is consistent with the observed atomic distribution and thermal parameter changes at each

lithium site. Thus the LGPS-type structure is evidently well-suited to three-dimensional conduction. Even though one-dimensional conduction is dominant at lower temperatures, the conduction pathway associated with Li1 and Li4 sites over the *ab* plane becomes evident at high temperatures. These conduction behaviors are also consistent with the previously reported results of MD simulation studies.²³ Isotropic ionic diffusion in a solid electrolyte is favorable in terms of practical application of the material in an all solid-state battery, since anisotropic ionic diffusion may prevent high ionic diffusion between the electrolyte and the electrode particles and thus reduce the ability of the solid-state cell to generate current. The LGPS structure is therefore suitable for practical applications, such as in all solid-state batteries.

Conclusions

A solid solution of the lithium superionic conductor $\text{Li}_{10+\delta}\text{Ge}_{1+\delta}\text{P}_{2-\delta}\text{S}_{12}$ ($0 \leq \delta \leq 0.35$) was synthesized and its structure and ionic conductivity were determined. An ionic conductivity value of $1.42 \times 10^{-2} \text{ S cm}^{-1}$ was obtained at 300 K for sintered pellets of the sample in which $\delta = 0.35$. The Arrhenius plots of the conductivity show a change in slope at high temperatures, at which the activation energy for ionic conduction decreases to approximately 10 kJ mol^{-1} , which is characteristic of highly ionic conducting solids. The ionic conduction mechanism determined by neutron diffraction measurements indicates a change in conduction pathway with increasing temperatures, such that a one-dimensional pathway transitions to a three-dimensional mechanism at elevated temperatures. The lithium diffusion pathway visualized through MEM analysis assisted in elucidating the conductivity pathway changes with temperature. The isotropic ionic conducting characteristics of the LGPS structure may mean that related structures of this material are suitable for practical applications in all-solid-state batteries.

Acknowledgements

This research was supported by the Post-LiEAD project of the New Energy and Industrial Technology Development Organization (NEDO), Japan. The program used for the MEM analysis was developed through the support of the RISING project of NEDO. Synchrotron and neutron radiation data were obtained through projects approved by the Japan Synchrotron Radiation Research Institute (JASRI) (Proposal Nos. 2011A1612 and 2011B1697) and the Japan Proton Accelerator Research Complex (J-Parc) (Proposal Nos. 2010B0065, 2012A0107, 2012B0110, and 2013A0133).

Notes and references

^a Department of Electronic Chemistry, Interdisciplinary Graduate School of science and Engineering, Tokyo Institute of Technology, 4259 Nagatsuta, Midori, Yokohama, Kanagawa 226-8502, Japan. (Fax: +81 45-924-5401, Tel: +81-45-924-5401, E-mail: kanno@echem.titech.ac.jp)

^b Battery Research Division, Higashifuji Technical Center, Toyota Motor Corporation, 1200 Mishuku, Susono, Shizuoka 410-1193, Japan.

^c Neutron Science Laboratory, Institute of Materials Structure Science, High Energy Accelerator Research Organization (KEK), 1-1 Oho, Tsukuba, Ibaraki 305-0801, Japan

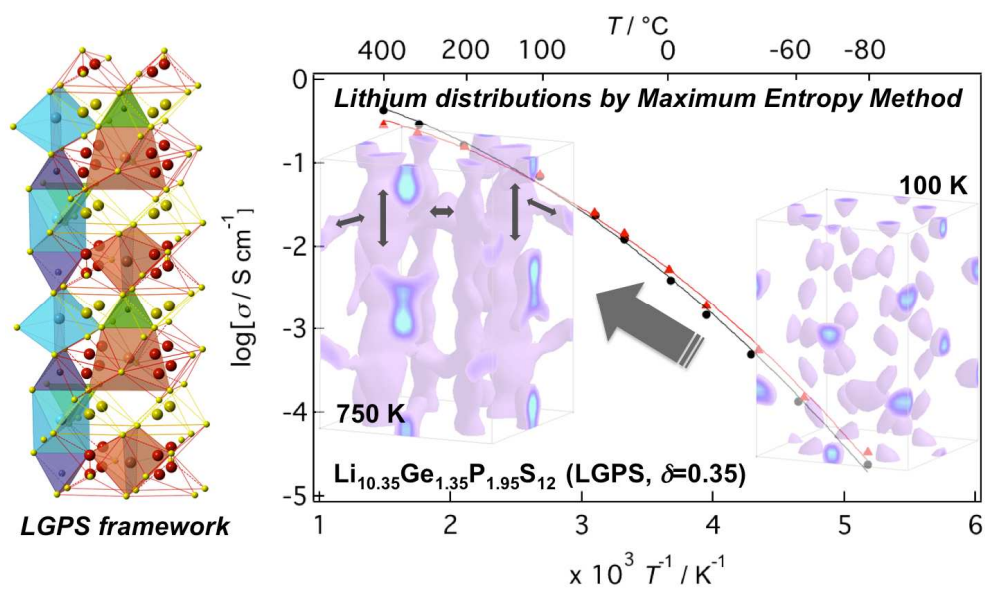
† Electronic Supplementary Information (ESI) available: [details of any supplementary information available should be included here]. See DOI: 10.1039/b000000x/

- X. Xu, K. Takada, K. Watanabe, I. Sakaguchi, K. Akatsuka, B. T. Hang, T. Ohnishi and T. Sasaki, *Chem. Mater.*, 2011, **23**, 3798.
- Y. Kato, K. Kawamoto, R. Kanno and M. Hirayama, *Electrochemistry*, 2012, **80**, 749.
- T. Ohtomo, A. Hayashi, M. Tatsumisago, Y. Tsuchida, S. Hama and K. Kawamoto, *J. Power Sources*, 2013, **233**, 231.
- N. Kamaya, K. Homma, Y. Yamakawa, M. Hirayama, R. Kanno, M. Yonemura, T. Kamiyama, Y. Kato, S. Hama, K. Kawamoto and A. Mitsui, *Nat. Mater.*, 2011, **10**, 682.
- P. E. Stallworth, J. J. Fontanella, M. C. Wintersgill, C. D. Scheidler, J. J. Immel, S. G. Greenbaum and A. S. Gozdz, *J. Power Sources*, 1999, **81–82**, 739.
- B. Garcia, S. Lavallée, G. Perron, C. Michot and M. Armand, *Electrochimica Acta*, 2004, **49**, 4583.
- F. Du, X. Ren, J. Yang, J. Liu and W. Zhang, *The J. Phys. Chem. C*, 2014, **118**, 10590.
- Y. Mo, S. P. Ong and G. Ceder, *Chem. Mater.*, 2012, **24**, 15.
- P. Bron, S. Johansson, K. Zick, J. Schmedt auf der Gunne, S. Dehnen and B. Roling, *J. Am. Chem. Soc.*, 2013, **135**, 15694.
- Y. Kato, R. Saito, M. Sakano, A. Mitsui, M. Hirayama and R. Kanno, *J. Power Sources*, 2014, **271**, 60.
- S. Hori, K. Suzuki, M. Hirayama, Y. Kato, T. Saitoo, M. Yonemura and R. Kanno, *Faraday Discussions*, 2014, Accepted
- A. Kuhn, O. Gerbig, C. Zhu, F. Falkenberg, J. Maier and B. V. Lotsch, *Phys. Chem. Chem. Phys.*, 2014, **16**, 14669.
- S. Torii, M. Yonemura, T. Yulius Surya Panca Putra, J. Zhang, P. Miao, T. Muroya, R. Tomiyasu, T. Morishima, S. Sato, H. Sagehashi, Y. Noda and T. Kamiyama, *J. Phys. Soc. Jpn*, 2011, **80**, SB020.
- T. Ishigaki, A. Hoshikawa, M. Yonemura, T. Morishima, T. Kamiyama, R. Oishi, K. Aizawa, T. Sakuma, Y. Tomota, M. Arai, M. Hayashi, K. Ebata, Y. Takano, K. Komatsuzaki, H. Asano, Y. Takano and T. Kasao, *Nucl. Inst. Meth. Phys. Res. A*, 2009, **600**, 189.
- R. Oishi, M. Yonemura, Y. Nishimaki, S. Torii, A. Hoshikawa, T. Ishigaki, T. Morishima, K. Mori and T. Kamiyama, *Nuclear Instruments and Methods in Physics Research Section A: Accelerators, Spectrometers, Detectors and Associated Equipment*, 2009, **600**, 94.
- F. Izumi and K. Momma, *Journal of the Vacuum Society of Japan*, 2010, **53**, 706.
- F. Izumi and K. Momma, *Solid State Phenomena*, 2007, **130**, 15.
- Zhang, J.; Kiyonagi, R.; Yonemura, M.; Ishikawa, Y.; and Kamiyama, T. Z-MEM, Textbook of Z-Code Powder diffraction data analysis school, Tokyo, Japan, Mar 25-26, 2014.
- Ishikawa, Y.; Yonemura, M.; and Kamiyama, T. Z-3D, Textbook of Z-Code Powder diffraction data analysis school, Tokyo, Japan, Mar 25-26, 2014.
- R. D. Shannon and C. T. Prewitt, *Acta Crystallographica Section B*, 1969, **25**, 925.
- West, A. R. In *Solid State Chemistry and Its Applications*, 2nd ed; John Wiley & Sons: Chichester, U. K., 1988; Chap. 13.3.2; p. 482

Journal Name

22. A. V. Chadwick, *Solid State Ionics*, 1983, **8**, 209.
23. S. Adams and R. Prasada Rao, *J. Mate. Chem.*, 2012, **22**, 7687.
24. A. Kuhn, J. Kohler and B. V. Lotsch, *Phys. Chem. Chem. Phys.*, 2013, **15**, 11620.

Table of Contents



The lithium diffusion pathway in the LGPS structure visualized through MEM analysis assisted in elucidating the conductivity pathway changes with temperature.